PHYSICAL REVIEW MATERIALS **7**, L110401 (2023)

Letter

Local-concentration-based descriptor predicting the stacking fault energy of refractory high-entropy alloys

Cong Ma and Wang Gao [*]

Key Laboratory of Automobile Materials, Ministry of Education, Department of Materials Science and Engineering, Jilin University, 130022 Changchun, China

(Received 4 April 2023; accepted 11 October 2023; published 22 November 2023)

Refractory high-entropy alloys (RHEAs) show the potential for high-temperature structural materials, but their brittleness and low ductility at room temperature prohibit the processing and further practical applications, which can be characterized by the generalized stacking fault energy (GSFE). However, the local chemical environment varies significantly across parallel GSF planes, resulting in a substantial fluctuation of GSFE values rather than a unique value, which manifests the local nature of GSFE. We proposed an effective descriptor based on the local concentration ratio near the GSF to quantitatively predict the local GSFE of RHEAs. We find that the role of a given element in determining GSFE strongly depends on its valence-electron number relative to other components and the contribution of its *s* and *d* electrons to its cohesive properties. Notably, the descriptor not only unifies the local nature of GSFE from simple alloys to RHEAs but also helps to quickly design RHEAs as the involved parameters are easily accessible.

DOI: 10.1103/PhysRevMaterials.7.L110401

Introduction. Since first proposed by Senkov *et al.* in 2010 [1], refractory high-entropy alloys (RHEAs) serve as a candidate for high-temperature structural materials, excelling over conventional Ni-based superalloys [2], which have potential applications in gas turbines and aircraft [3,4]. However, the bcc RHEAs show brittleness (i.e., low ductility) at room temperature, making them hard to process and for use in further practical applications [4,5]. The generalized stacking fault energy (GSFE) [6], which is defined as the energy cost when shifting one part of a crystal with respect to the other along the slip direction on the slip planes, determines the ability of plastic deformation [7–9] and also enters the Rice criterion for characterizing ductility [7,10,11]. In simple binary alloys, the trend of GSFE can be rationalized by the Suzuki mechanism [12–14]. However, when extended to complex HEAs, such as RHEAs [1,2,5,15–17], the conventional Suzuki mechanism is generally considered invalid [18,19]. The complexity of HEAs originating from the random distribution of multielements prohibits the establishment of the structure-property relationship of GSFE.

Uncovering the intrinsic determinants is the prerequisite to building a predictive descriptor. The attempts can be traced back to the conventional Suzuki mechanism of simple alloys—the aggregation of solute atoms in the stacking fault lowers the stacking fault energy (SFE) [12–14]. This mechanism is based on the concept of local concentration, which refers to the compositional fluctuation near the GSF planes (that may extend several planes outward) [20,21]. The correlation of local concentration to GSFE has been extended to medium-entropy alloys (e.g., CrCoNi and MoNbTi) and HEAs (e.g., CrMnFeCoNi) [22,23]. Nonetheless, no quantitative relationship between GSFE and local concentration has been established. For example, the increase of GSFE with local Ni content (i.e., Ni aggregation) in the CrCoNi and CrMnFeCoNi shows a highly nonlinear behavior [22]. For the MoNbTi, the correlation refers to the monotonic increase of GSFE with Mo aggregation in a certain range [23]. Although there are many other descriptors, such as the short-range order (SRO) [24–26], concentration wave (CW) [27–29], and global concentration (i.e., compositional proportion) [21,28,30–35], they are mainly focused on the fcc HEAs, and little is known about the bcc RHEAs.

In bcc RHEAs, due to the difference of chemical composition in parallel GSF planes within the same slip plane, such as {110}, the GSFE values vary significantly across different GSF planes, which further manifests the local nature of GSFE [36,37]. This point is also found in fcc HEAs, such as the CrCoNi and NiFeCr HEAs [24,35]. However, the available descriptors in the fcc HEAs, such as the SRO [24], CW [29], and global concentration [35], describe the global properties of a HEA configuration and are correlated with statistically averaged GSFE from different GSF planes. Therefore, they show an intrinsic drawback in accounting for the local GSFE and thus are limited to qualitative correlation, rather than point-to-point prediction (i.e., the one-to-one mapping of GSF with its GSFE).

Herein, we proposed a local-concentration-based descriptor to quantitatively predict the GSFE of RHEAs. A given element behaves substantially differently in different RHEAs, depending on its valence-electron number relative to other components and its *s* and *d* components of cohesive energies. In addition, the model with obtainable parameters provides a fast way to screen the HEAs with desirable mechanical properties.

---

[*] wgao@jlu.edu.cn

Methods

a. Structures. The bcc RHEAs, an important but less-studied group of HEAs, contain four to nine elements in the compositional space of IV B (i.e., Ti, Zr, and Hf), V B (i.e., V, Nb, and Ta), VI B (i.e., Cr, Mo, and W), and Al elements [1,2,5,15–17]. Herein, we adopted five quinary RHEAs, TiVNbTaMo, TiVNbTaW, ZrVNbTaMo, HfVNbTaMo, and TiNbTaMoW; six quaternary RHEAs, TiNbTaMo, VNbTaMo, VNbTaW, NbTaMoW, ZrVNbTa, and HfVNbTa; and two nonequimolar RHEAs, $TiNbTaMo_2$ and $TiNbTa_2Mo$. All the bcc RHEA structures are generated with the special quasirandom structure method in the Alloy Theoretic Automated Toolkit (ATAT) code [38]. The default supercells contain 60 atoms. We test the convergence of GSFE to the size of the supercell by using 120-atom supercells (see the details in Supplemental Material Note 1 [39]). The super large supercells with 960 atoms are also used to simulate the realistic RHEAs with the possible randomness of components [35]. In addition, the calculations for all transition metals (TMs) are conducted with their most stable crystal structures, i.e., bcc, fcc, and hcp.

b. Computational parameters. The density functional theory (DFT) calculations with the 60- or 120-atom supercells are performed in VASP code with the recommended projector augmented-wave potentials [40,41]. The same energy cutoff of 400 eV is used throughout for the comparison of different RHEA systems. Non-spin-polarized calculations are used throughout, since all the elements involved are nonmagnetic. The geometric relaxation is performed at the Perdew-Burke-Ernzerhof level of theory [42], converged within 10^{-6} eV and 0.02 eV/Å for the electronic and ionic relaxation, respectively. The first-order Methfessel-Paxton smearing of 0.2 eV and the R_k length for gamma-centered k-point meshing at ∼30 Å is used to get well-converged results. The computations with the 960-atom supercells are conducted with the moment tensor potential (MTP) machine learning force field (MLFF) implemented in the LAMMPS code [23,43,44].

c. Generalized stacking fault energy. The shear method is used to generate structures with GSF, without introducing a vacuum and with fewer atoms in the supercell, compared with the slab method [7,22,45]. The optimal lattice parameters are fitted according to the equation of state. For the $\langle 111\rangle\{110\}$ slip system, all the atoms are only allowed to relax normally to the $\{110\}$ plane with the supercell fixed. The results with the constrained relaxation must lie in between the simple shear (without relaxation) and pure shear (relaxing both atomic position and cell) [46].

The GSFE is defined as follows:

$$\gamma_{\mathrm{gsf}} = \frac{E_{\mathrm{gsf}} - E_{pf}}{A}, \tag{1}$$

where E_{gsf} are the energies of RHEA with one GSF plane in each supercell, E_{pf} are the energies of perfect RHEA, and A is the area of the GSF plane. The GSFE in the most possible $\langle 111\rangle\{110\}$ slip system of the bcc crystal shows one maximum peak at $\sim 1/4\langle 111\rangle$, which is referred to as unstable SFE (USFE; γ_{usf}) [36,47,48]. For the TMs with bcc, fcc, and hcp crystal structures, the stacking fault energy is unified as γ_{sf}.

Results and discussion

a. The descriptor based on the local concentration. Inspired by the correlation of GSFE to the local concentration, we plot the GSFE against the number of Mo/Ti/V/Nb/Ta in the first-near GSF (i.e., the two layers of atoms involved in the GSF) in Fig. 1. The increase of Mo content (i.e., Mo aggregation) raises GSFE, while the increase of Ti content (i.e., Ti aggregation) lowers GSFE just like the conventional Suzuki effect. For the correlation, Mo is the strongest, followed by Ti [see Figs. 1(a) and 1(b)], and the other three (i.e., V, Nb, and Ta) are the weakest [see Figs. 1(c)–1(e)]. These results demonstrate the predominant role of Mo and Ti concentrations in determining the GSFE. We manually construct the first-near GSF with high Mo content, and good linearity still exists for the Mo and Ti, further manifesting their predominant role (see Supplemental Material Fig. S1 [39]). When extended to the second-near GSF, however, the linearity significantly decreases for Mo but slightly increases for Ti (see Fig. S2 [39]), which means that the effect of Mo is more localized than Ti. Nevertheless, the GSFE is widely distributed at a certain Mo concentration, which is more prominent for Ti. The results further identify the literature findings that the correlation between GSFE and an individual concentration fails to estimate GSFEs quantitatively [22,23].

Considering the opposite trend of Mo and Ti concentrations with GSFE, we test four formulations in the TiVNbTaMo system by including the first- and second-near Mo/Ti concentrations [see Figs. 2(a)–2(d)]. The results show that further including the Mo atoms of the second-near GSF always leads to poor linearity. However, further including the Ti of the second-near GSF improves the linearity. We also test the weighting factor of Ti content in the second-near GSF for the TiVNbTaMo and TiVNbTaW HEAs [see Figs. 2(e) and 2(f)]. The fitting coefficient R^2 peaks at the weighting factor of 0.5. As a result, the descriptor, local concentration ratio (D_{lcr}), is settled as follows:

$$D_{\mathrm{lcr}} = \frac{\sum C_{VE\,\mathrm{most},1}}{\sum C_{VE\,\mathrm{least},1} + 0.5\sum C_{VE\,\mathrm{least},2}}, \tag{2}$$

where the $C_{VE\,\mathrm{most}/VE\,\mathrm{least},1/2}$ is the concentration of elements with the most/least valence electrons within the first-/second-near GSFs (i.e., Mo and Ti for TiVNbTaMo HEAs). The second-near GSF refers to the two layers that extend outward from the first-near GSF [20]. The weighting factor 0.5 means that for the element with the least valence electron, the concentration of the second-near GSF ($C_{VE\,\mathrm{least},2}$) has a smaller contribution compared with that of the first-near GSF ($C_{VE\,\mathrm{least},1}$), but is indispensable for quantitative prediction.

As a result, the GSFE shows rather good linearity with the proposed descriptor D_{lcr} [see Fig. 3(a)]. The mean absolute error (MAE) is ∼39.02 mJ/m^2, with the R^2 as high as 0.820, in contrast to the 0.676 and 0.351 for Mo and Ti concentration, respectively [see Figs. 1(a) and 1(b)]. Notably, here we show that a single descriptor, based on the local concentration, realizes the point-to-point quantitative predictions for GSFEs.

b. The role of different elements. To identify the role of different elements in the GSFE of RHEAs, we adopted three strategies: substituting one element with another; removing one element; changing the atomic proportion (i.e., deviating from equimolar).

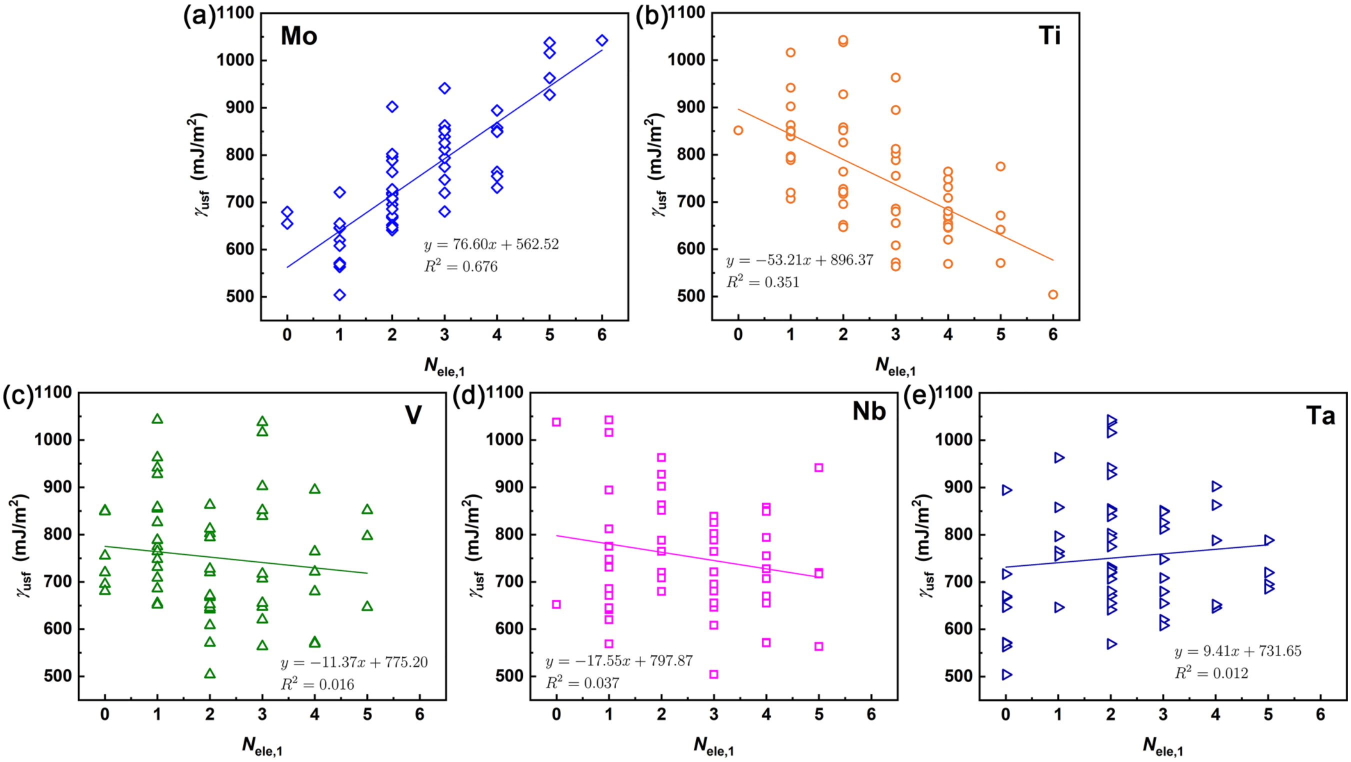

FIG. 1. The USFE (γ_{usf}) as a function of the number of elements in the first-near GSF ($N_{\mathrm{ele},1}$): Mo (a), Ti (b), V (c), Nb (d), and Ta (e).

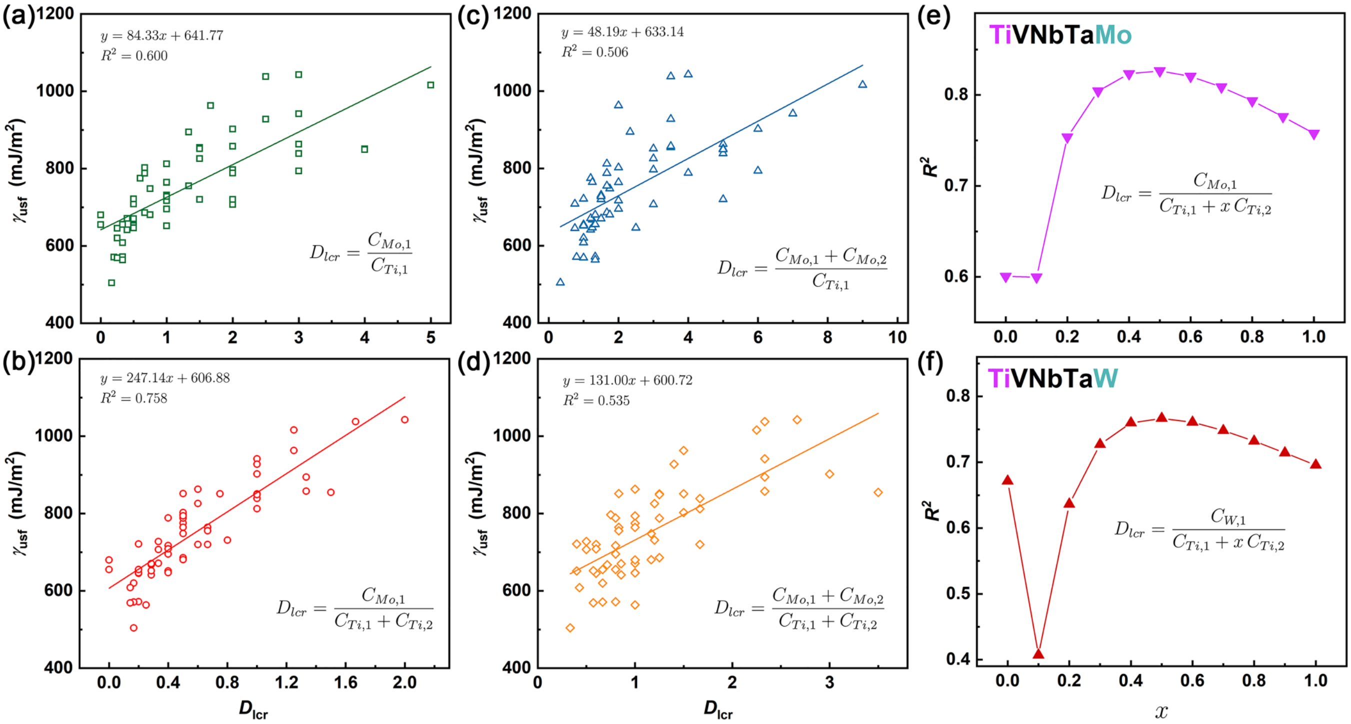

FIG. 2. The USFE (γ_{usf}) against the descriptor D_{lcr} with different formulations. For TiVNbTaMo (a)–(e) and TiVNbTaW (f) RHEAs, Mo and W show the most valence electrons, while Ti shows the least. The $C_{\mathrm{Mo/W/Ti},1}$ and $C_{\mathrm{Mo/W/Ti},2}$ refer to the concentrations of Mo/W/Ti atoms in the first- and second-near GSFs, respectively. (e) and (f) The fitting coefficient R^2 as a function of the weighting factor (x) for the $C_{\mathrm{Ti},2}$. The R^2 peaks at the weighting factor of 0.5 for both the TiVNbTaMo (e) and the TiVNbTaW (f), which means that the second-near concentration effect of Ti is small weighted but plays an important part in quantitatively predicting USFEs.

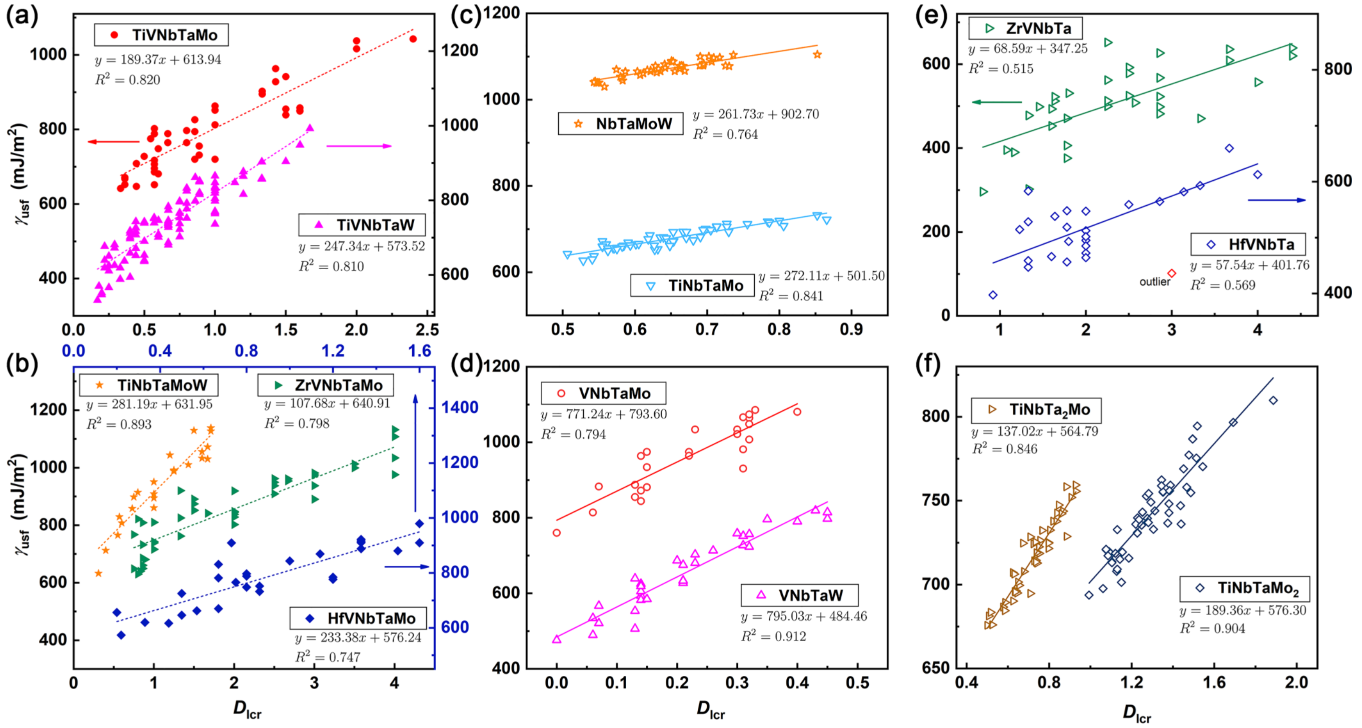

FIG. 3. The USFE (γ_{usf}) against the descriptor D_{lcr} in the RHEAs. (a) TiVNbTaMo and TiVNbTaW. (b) ZrVNbTaMo, HfVNbTaMo, and TiNbTaMoW. (c) TiNbTaMo (Group I) and NbTaMoW (Group II). (d) VNbTaMo and VNbTaW (Group II). (e) ZrVNbTa and HfVNbTa (Group III). (f) Nonequimolar $TiNbTaMo_2$ and $TiNbTa_2Mo$. The results in (c) and (f) are from the MTP MLFF with the 960-atom supercells [23,43], while the rest are from the DFT method with the 60-atom supercell.

The proposed descriptor D_{lcr} is still applicable to determine GSFE when Mo of TiVNbTaMo is substituted by W, i.e., TiVNbTaW, or when Ti of TiVNbTaMo is substituted by Zr/Hf, i.e., ZrVNbTaMo, and HfVNbTaMo [see Figs. 3(a) and 3(b)]. These results demonstrate the elements with the same number of valence electrons (namely, in the same group) follow a similar rule in determining GSFE. When substituting V with W in the TiVNbTaMo, Mo and W with an identical number of valence electrons still play a similar role and work together in an additive way to determine GSFE [see Fig. 3(b)]. The results of substitutions demonstrate that the number of valence electrons plays an essential role in predicting GSFEs of RHEAs: the elements with the most and least valence electrons in RHEAs predominate.

We remove one element in the above quinary RHEAs (TiVNbTaMo, TiVNbTaW, ZrVNbTaMo, HfVNbTaMo, and TiNbTaMoW): the first one is to remove one V B element (i.e., V, Nb, and Ta; labeled as Group I); the second is with IV B elements absent (i.e., Ti, Zr, and Hf; labeled as Group II); the third is with VI B elements absent (i.e., Mo and W; labeled as Group III) [see Figs. 3(c)–3(e)]. For Group I, removing V from TiVNbTaMo to obtain TiNbTaMo, D_{lcr} still linearly scales with GSFE [see Fig. 3(c)], with R^2 up to 0.84. The similarity further demonstrates that the elements with the number of valence electrons between the most and least play a negligible role. However, removing Ti from the TiVNbTaMo, TiVNbTaW, and TiNbTaMoW to obtain VNbTaMo, VNbTaW, and NbTaMoW [see Figs. 3(c) and 3(d)], the V, Nb, and Ta show the least valence electrons and thus take the role of former Ti in determining GSFE, entering the denominator of the D_{lcr} expression. When removing Mo from ZrVNbTaMo and HfVNbTaMo to obtain ZrVNbTa and HfVNbTa [see Fig. 3(e)], the V, Nb, and Ta have the most valence electrons, taking the role of the former Mo and entering the numerator of the D_{lcr} expression. These results demonstrate that for a given element in HEAs (such as V), its influence on GSFE strongly depends on the elemental composition of RHEAs: when it has the most valence electrons, it increases GSFE; when it has the least, it decreases GSFE; however, when it has the number of valence electrons between the most and least, it contributes slightly to GSFE.

We also adopt the nonequimolar RHEAs, such as $TiNbTaMo_2$ and $TiNbTa_2Mo$ [see Fig. 3(f)]. The descriptor D_{lcr} linearly scales with the GSFE, like its equimolar counterpart TiNbTaMo, What is obvious is that the variation in the proportion of elements changes the local concentration, as well as the slope and intercept of the linear relationship. However, it does not impair good linearity. All the findings demonstrate that our descriptor quantitatively captures the local-concentration-based nature of the GSFEs in the RHEAs and reveals the role of any given element in determining the GSFEs.

In the complex RHEAs, our results indicate that the number of valence electrons still serves as an important parameter in identifying the role of different elements, just like in binary dilute alloys, but the intrinsic determinant of GSFEs is the corresponding elemental concentration, rather than the number of valence electrons. In dilute binary alloys, such as Nb- and

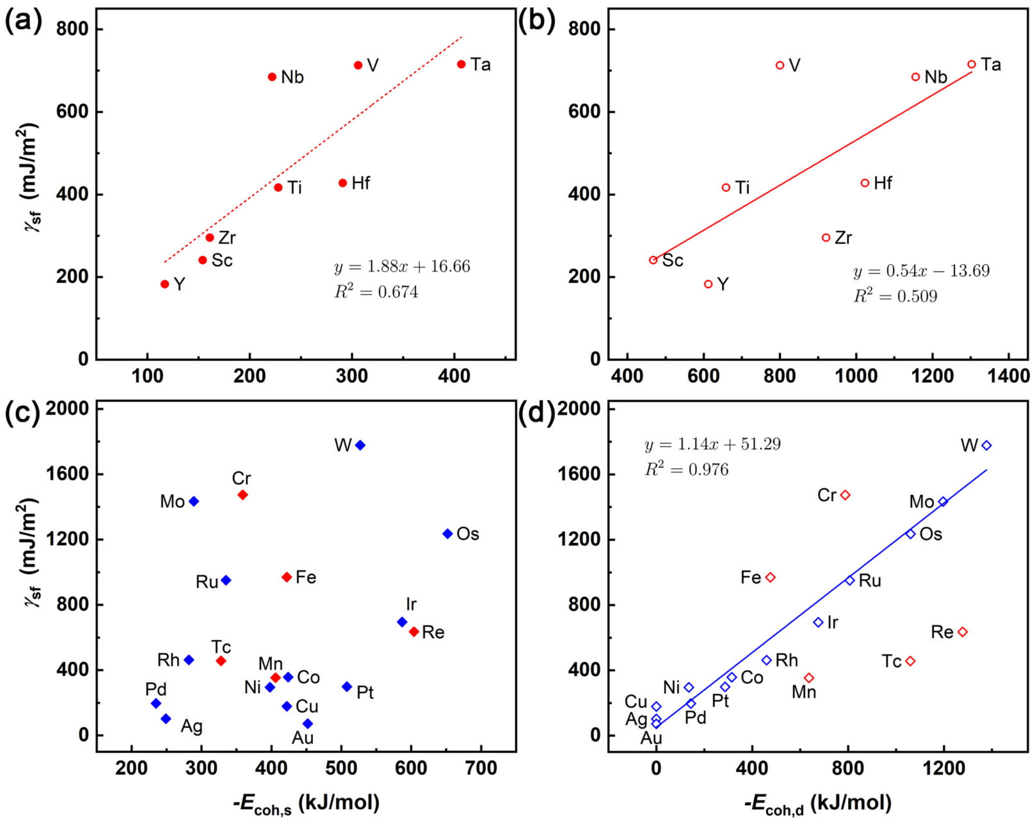

FIG. 4. The GSFE (γ_{sf}) against the cohesive energy (E_{coh}) for early and late transition metals (TMs). (a) and (b) The GSFE (γ_{sf}) against the contribution of s and d electrons to the cohesive energy ($E_{\mathrm{coh},s}$ and $E_{\mathrm{coh},d}$) for the early TMs. (c) and (d) The GSFE (γ_{sf}) against the $E_{\mathrm{coh},s}$ and $E_{\mathrm{coh},d}$ for the late TMs. The Cr, Fe, Mn, Tc, and Re are outliers. Data of $E_{\mathrm{coh},s}$ and $E_{\mathrm{coh},d}$ are from Ref. [49].

Mg-based alloys, the trend of GSFE has been correlated with the valence-electron difference or size difference compared with the matrix element [46,50–52]. This is because the denser charge density with more valence electrons means stronger bonding and thus hinders the formation of GSF by shearing [46]. In contrast, the size difference has little effect on the GSFE of RHEAs: the Zr and Hf atoms have larger atomic radii than others by about 8%–20% (according to the atomic radius listed in Ref. [15]), but the scaling relation between GSFE and D_{lcr} remains good when substituting Ti with Zr or Hf [see Figs. 3(a) vs 3(b)].

c. The physical origin of the model

1. The localized and delocalized characteristics. We try to understand the physical origin of the descriptor D_{lcr} with the cohesive energy E_{coh}: GSFE $\sim D_{\mathrm{lcr}} \sim E_{\mathrm{coh}}$. Intuitively, the strong cohesion means the large resistance of deformation to form a GSF (i.e., shifting one part of the crystal with respect to the other), leading to GSFE $\propto E_{\mathrm{coh}}$. A good scaling relation of GSFE and E_{coh} has been found in hcp metals [53]. We demonstrate that the scaling relation still exists for all TMs splitting into the two groups—one is the early TMs, and the other is the rest removing the Cr, Fe, Mn, Tc, and Re outliers (see Fig. 4). Moreover, in γ-Fe-Mn and Ti-Al alloys, the cohesive energy follows the same trend as SFE towards the change of concentration, further demonstrating the correlation between E_{coh} and GSFE [54,55].

Based on the close correlation between GSFE and E_{coh}, we try to understand why the elements with the least valence electrons play a more delocalized role than those with the most valence electrons. According to the tight-binding model [49,56–58], the d electrons mainly control the variation of the cohesive energy from one TM to the next, while the contribution of s electrons to the cohesive energy ($E_{\mathrm{coh},s}$) is small and can be approximately considered constant due to the half-filled s-band filling. However, when including $E_{\mathrm{coh},s}$ via the free-electron approximation in the Friedel model, the results show that $E_{\mathrm{coh},s}$ follows the same trend as the total E_{coh} for the early TMs, i.e., Sc/Y/La, Ti/Zr/Hf, and V/Nb/Ta. This indicates that the s electrons play an important role in determining the trend of E_{coh} for the early TMs [49]. Accordingly, for early TMs, $E_{\mathrm{coh},s}$ exhibits much better linearity with GSFE than $E_{\mathrm{coh},d}$ [see Figs. 4(a) vs 4(b)]. There is no surprise that for the late TMs, the GSFE scales well with $E_{\mathrm{coh},d}$ but not $E_{\mathrm{coh},s}$ [see Figs. 4(c) vs 4(d)]. These results demonstrate that the s electrons play an important part in determining GSFE for Ti, Zr, and Hf, while the d electrons predominate in Mo and W. Since the s and d electrons show nonlocal and local characteristics respectively, the influence of Ti, Zr, and Hf on the bonding of RHEAs is more delocalized than that of Mo and W. Therefore, the descriptor D_{lcr} includes the concentration effect of both the first- and second-near GSFs of Ti/Zr/Hf but only that of the first-near GSF of Mo/W.

2. The role of valence-electron number. Finally, we try to understand why the number of valence electrons serves as a criterion to select elements for including their concentrations in the descriptor D_{lcr}. This can be rationalized by the change

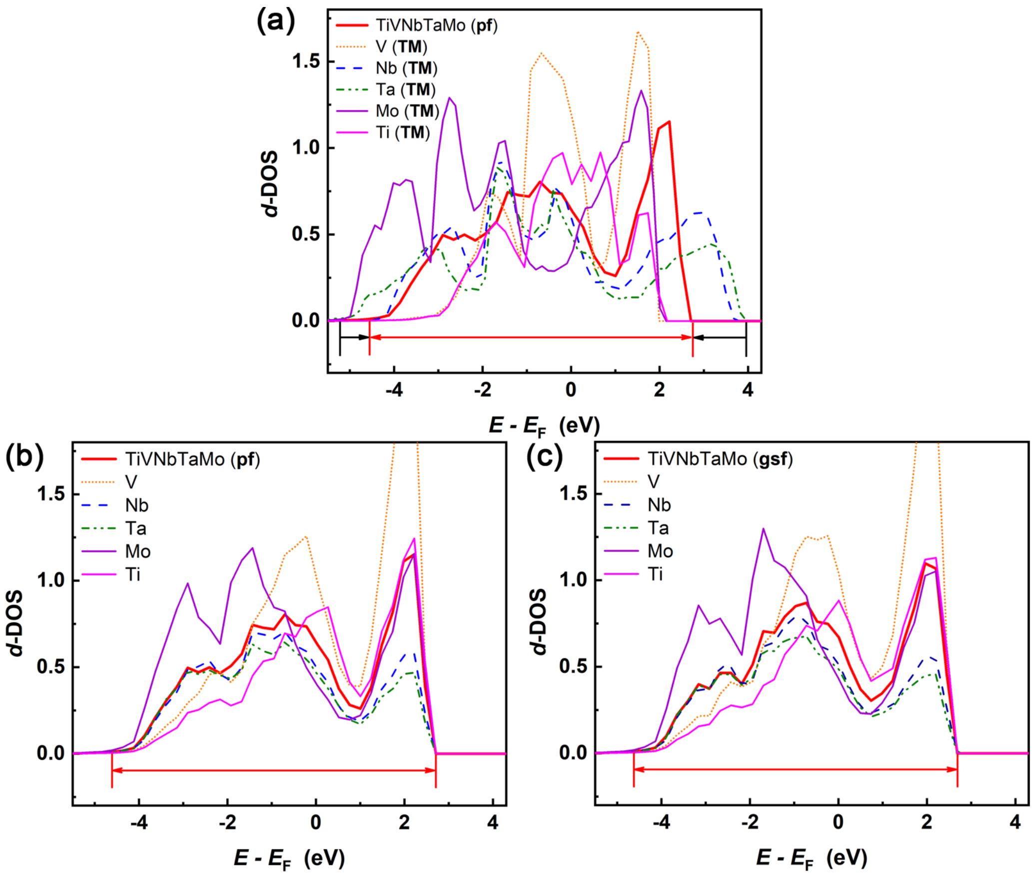

FIG. 5. (a) The comparison of the density of states for d-bands (d-DOS) between TMs (i.e., V, Nb, Ta, Mo, and Ti) and perfect (pf) TiVNbTaMo HEA. (b) and (c) The comparison of the d-DOS between perfect (pf) and generalized-stacking-faulted (gsf) TiVNbTaMo RHEAs with their components (i.e., V, Nb, Ta, Mo, and Ti). The d-band width (W_d) and filling (N_d) per atom are listed in Table I.

in the density of states (DOS) of d-bands (d-DOS) from TMs to perfect (pf) to generalized-stacking-faulted (gsf) RHEAs, such as d-band width (W_d) and filling (N_d).

When forming TiVNbTaMo from TMs (i.e., V, Nb, Ta, Mo, and Ti), the d-DOS of TM elements with varying W_d have to reshape to adapt to a common W_d, as indicated by the arrows in Figs. 5(a) and 5(b). The numerical values are provided in Table I. For the TMs, the Ta has the largest W_d while the Ti has the smallest one. From TM to pf TiVNbTaMo, the W_d of Ta decreases significantly while that of Ti increases significantly, approaching the W_d of TiVNbTaMo. The averaging effect of W_d in HEAs can be traced back to simple binary alloys. A typical example is that the d-DOS for binary MoPd alloys is similar to that of Ru—the average element corresponding to MoPd [59]. In contrast, the d-band filling (N_d) remains almost unchanged when forming pf TiVNbTaMo from TMs (see Table I). The conservation of d-band filling (N_d) also has been demonstrated in the bimetallic surfaces, which is unaffected by the strain and ligand effects [60]. From the pf to gsf RHEAs, the change in both the W_d and N_d is even smaller [see pf vs gsf rows in Table I and Figs. 5(b) vs 5(c)]. Overall, the W_d becomes average from TMs to pf RHEAs but slightly changes from pf to gsf RHEAs, while the N_d maintains almost in three situations. These results may explain why the role of a given element in determining GSFE strongly depends on its valence-electron number (i.e., N_d), since different elements in the alloys can be distinguished by N_d, rather than W_d.

TABLE I. The variation of d-band width (W_d) and filling (N_d) for each element (V, Nb, Ta, Mo, and Ti) from transition metals (TMs), to perfect (pf) and generalized-stacking-faulted (gsf) TiVNbTaMo RHEAs. The results for TiVNbTaMo are the average over all atoms. The results validation is provided in Supplemental Material Note 2 [39].

		V	Nb	Ta	Mo	Ti	TiVNbTaMo
W_d (eV/atom)	TM	4.97	8.49	9.01	8.11	4.78	–
	pf	6.53	6.89	6.85	7.56	6.44	7.19
	gsf	6.42	6.81	6.79	7.48	6.34	7.08
N_d (e/atom)	TM	2.08	1.99	1.91	3.16	1.35	–
	pf	2.09	1.85	1.74	3.00	1.31	2.00
	gsf	2.16	1.87	1.76	3.05	1.35	2.04

In addition, the signature of d-DOS still plays a role in indicating the D_{lcr} as well as the USFE, like that in Ref. [61] where the electronic hybridization in the DOS explains the trend of cluster geometry of the secondary phase within a host metal. As shown in Figs. 6(a) and 6(b), with the increase of D_{lcr}, the d-DOS of pf TiVNbTaMo shifts leftward, while in the gsf TiVNbTaMo the shift is less noticeable. This means that the perfect TiVNbTaMo HEA grows more stable, making it hard to shift one part of the crystal with respect to the other to form a stacking fault and thus lead to a larger USFE.

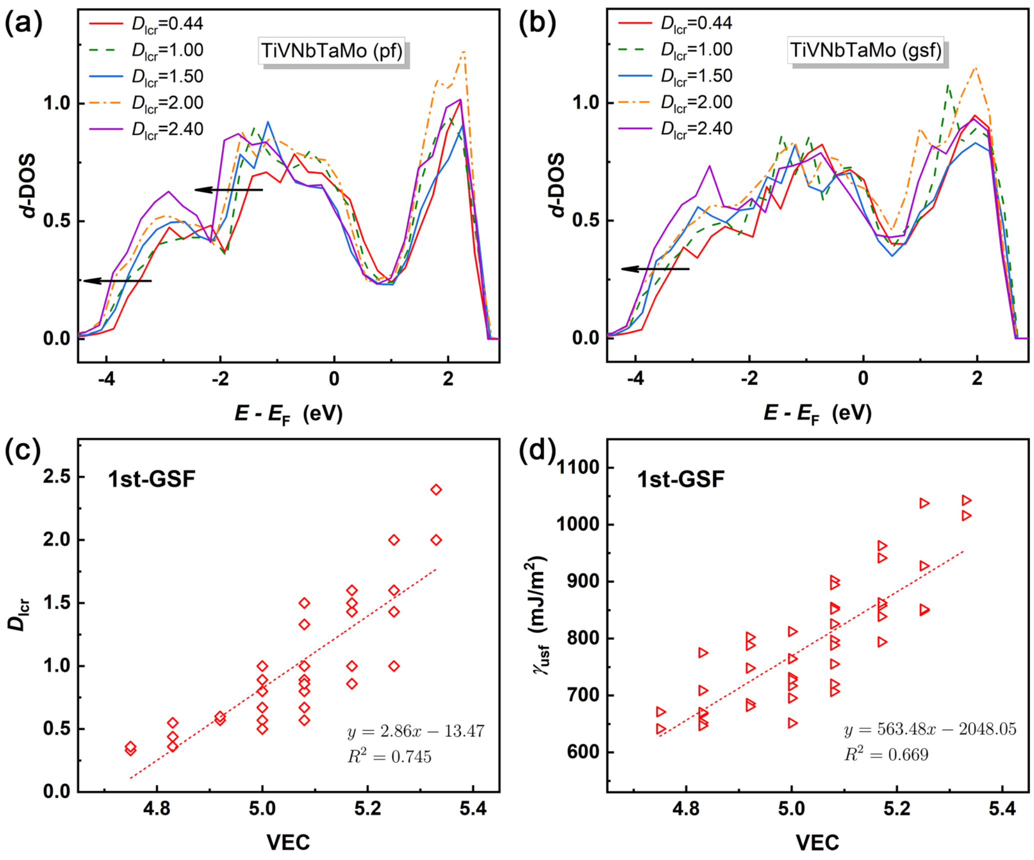

FIG. 6. (a) and (b) The density of states of *d*-bands (*d*-DOS) at different $D_{\rm lcr}$ for the perfect (pf) and generalized-stacking-faulted (gsf) TiVNbTaMo RHEAs. The *d*-DOS is the average over the total atoms of first-near GSF. (c) and (d) The $D_{\rm lcr}$ and USFE ($\gamma_{\rm usf}$) against the valence-electron concentration (VEC) in the first-near GSF of TiVNbTaMo RHEAs, compared with the $D_{\rm lcr} \sim \gamma_{\rm usf}$ in Fig. 3(a). The results for the first- and second-near GSFs are supplemented in Fig. S4.

The valence-electron concentration (VEC), defined as the average of the number of electrons over all atoms (unit: e/atom), accounts for the trend of $D_{\rm lcr}$ and USFE from the electronic perspective, just like the role of DOS in Ref. [61]. As shown in Figs. 6(c) and 6(d), the large VEC means a large $D_{\rm lcr}$ and USFE, and vice versa. Despite the simplicity and physical reasonableness, the VEC descriptor leads to multiple points at many VECs (i.e., many structures share the same VEC values) and thus is limited in quantitative predictions, compared with concentration ratio $D_{\rm lcr}$ in Fig. 3(a).

d. Successes and limitations. Apart from the clear physical picture, our model also shows the ability to realize point-to-point quantitative predictions. The MAE of all systems averages at 27.73 mJ/m^2, with the error below ∼4% in the range of GSFE between 400 and 1100 mJ/m^2 [see Fig. 7(a)]. The MAE lies between 5.21 and 49.71 mJ/m^2, with the error of each RHEA system ranging from 6.23% to 14.18%. For the RHEAs with 960-atom supercells, the MAEs are excellently low. For the RHEAs with 60-atom supercells, the large MAE can be greatly relieved by using larger supercells [20,21,24,35]. For example, the MAE reduces significantly from 39.02 (60 atoms) to 22.40 (120 atoms) for the TiVNbTaMo RHEAs, and from 33.73 (60 atoms) to 7.76 (960 atoms) for the TiNbTaMo RHEAs [see Figs. 7(b) and 7(c)].

Notably, the local-concentration-based descriptor $D_{\rm lcr}$ that realizes the point-to-point quantitative prediction further demonstrates the local property of GSFE. In contrast, the SRO and CW based on the global properties show an intrinsic drawback in accounting for the GSFE and thus are limited to qualitative correlation. Most importantly, our model is compatible with the conventional Suzuki mechanism (which is assumed to be out of date in HEAs) in determining the GSFE of RHEAs. In addition, the involved parameters of our model are easily accessible, and thus the model is more convenient for practical applications.

Apart from the commonly used elements in RHEA (i.e., Ti, Zr, Hf, V, Nb, Ta, Mo, and W), the addition of the costly Re element is promising to improve the ductility of alloys without sacrificing too much mechanical strength [9,62–64]. In our work, following the construction framework of $D_{\rm lcr}$ as shown in Fig. S5 (where Ti and Re have the least and most valence electrons, respectively), linearity between $D_{\rm lcr}$ and USFE still exists for the TiVNbTaRe but with a large MAE (56.49 mJ/m^2). The results show that the concentration-based descriptor $D_{\rm lcr}$ is general and captures the essential determinants of USFE where the elements with the most and least valence electrons predominate.

In addition, RHEAs may adopt dual-phase (such as particle phase or precipitation phase), instead of single ones [9,65].

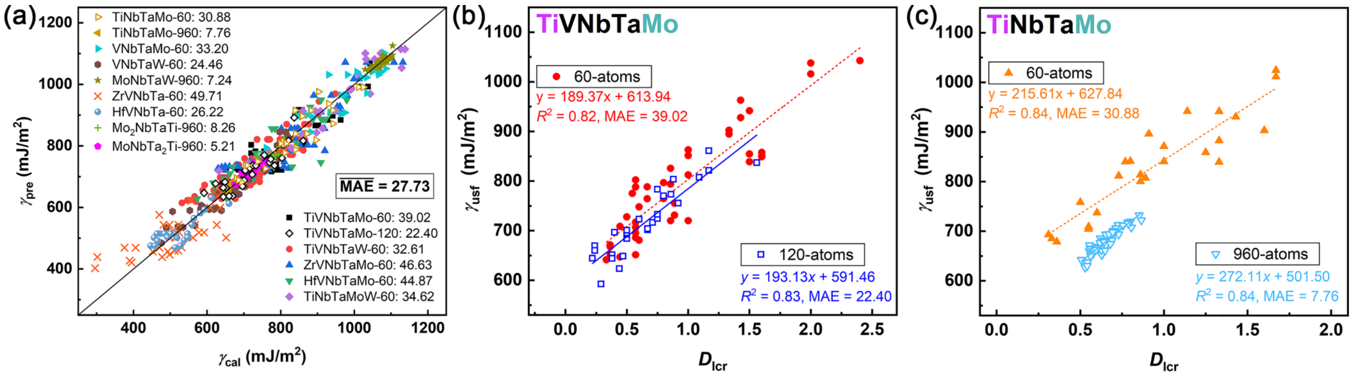

FIG. 7. (a) Comparison between the predicted (γ_{pre}) and the DFT/MLFF calculated ($\gamma_{\rm cal}$) USFEs for all RHEAs labelled with MAE. The 60, 120, and 960 refer to the number of atoms in the supercell. (b) For the TiVNbTaMo RHEAs with 60-atom and 120-atom supercells, the correlation between $\gamma_{\rm usf}$ and $D_{\rm lcr}$ is similar in the fitting coefficients (R^2), demonstrating that the good linearity has converged with respect to the sizes of supercell. The MAEs reduce significantly from small to large supercells. (c) For the TiNbTaMo RHEAs with 60 atoms and 960 atoms in the supercell. The situation is similar to the TiVNbTaMo RHEAs. The MAE greatly reduces using a 960-atom supercell.

The distribution of different phases complicates the situation, making it hard to figure out the underlying mechanism. What's more, simulating dual-phase needs a large supercell, and thus a reliable force field, such as the MTP MLFF (only for Ti, Nb, Ta, Mo, and W), is imperative, which is beyond the scope of the current study. In this work, we constrain to the single phase, leaving the complication for further study.

Conclusion. In summary, we proposed an effective descriptor for determining the GSFE of RHEAs, using the local concentration ratio of components with the most different number of valence electrons. The descriptor correlates with the individual local GSFE and realizes the point-to-point quantitative prediction for the GSFEs of RHEAs. We find that for a given RHEA, the elements with the most and least valence electrons play a determining role in the GSFEs, while the elements in between have a little contribution. The elements with the least valence electrons act in a more delocalized way than the elements with the most valence electrons because the former's s component of cohesive energy plays a part in their bonding variation. Notably, our model rebuilds the framework of the conventional Suzuki mechanism (that is generally considered invalid in HEAs) in determining the GSFE of RHEAs, and its local nature essentially excels over the models based on the global SRO and CW. In addition, the involved parameters of our model are easily accessible, and thus the model is more convenient for practical applications.

Acknowledgments. This work was supported by the National Natural Science Foundation of China (Grants No. 22173034, No. 11974128, and No. 52130101), the Opening Project of State Key Laboratory of High Performance Ceramics and Superfine Microstructure (SKL202206SIC), the Program of Innovative Research Team (in Science and Technology) in University of Jilin Province, the Program for JLU (Jilin University) Science and Technology Innovative Research Team (Grant No. 2017TD-09), the Fundamental Research Funds for the Central Universities, and the computing resources of the High Performance Computing Center of Jilin University, China.

---

[1] O. Senkov, G. Wilks, D. Miracle, C. Chuang, and P. Liaw, Refractory high-entropy alloys, Intermetallics **18**, 1758 (2010).

[2] O. N. Senkov, G. G. Wilks, J. M. Scott, and D. B. Miracle, Mechanical properties of $Nb_{25}Mo_{25}Ta_{25}W_{25}$ and $V_{20}Nb_{20}Mo_{20}Ta_{20}W_{20}$ refractory high entropy alloys, Intermetallics **19**, 698 (2011).

[3] S. W. McAlpine, J. V. Logan, and M. P. Short, Predicting single phase stability and segregation in the NbMoTaTi–(W, V) high entropy alloy system with the vacancy exchange potential, Scr. Mater. **191**, 29 (2021).

[4] Y. Zhang, T. T. Zuo, Z. Tang, M. C. Gao, K. A. Dahmen, P. K. Liaw, and Z. P. Lu, Microstructures and properties of high-entropy alloys, Prog. Mater. Sci. **61**, 1 (2014).

[5] E. P. George, D. Raabe, and R. O. Ritchie, High-entropy alloys, Nat. Rev. Mater. **4**, 515 (2019).

[6] V. Vitek, Intrinsic stacking faults in body-centred cubic crystals, Philos. Mag. **18**, 773 (1968).

[7] Y.-J. Hu, A. Sundar, S. Ogata, and L. Qi, Screening of generalized stacking fault energies, surface energies and intrinsic ductile potency of refractory multicomponent alloys, Acta Mater. **210**, 116800 (2021).

[8] S. Shi, L. Zhu, H. Zhang, and Z. Sun, Strength and ductility of niobium alloys with nonmetallic elements: A first-principles study, Mater. Lett. **189**, 310 (2017).

[9] J. Qian, C. Wu, J. Fan, and H. Gong, Effect of alloying elements on stacking fault energy and ductility of tungsten, J. Alloys Compd. **737**, 372 (2018).

[10] J. R. Rice, Dislocation nucleation from a crack tip: An analysis based on the Peierls concept, J. Mech. Phys. Solids **40**, 239 (1992).

[11] X. Yao, Y. Mao, and Y.-F. Guo, Effects of alloying elements on the generalised stacking fault energies of Pt: A first-principles study, Philos. Mag. **101**, 1033 (2021).

[12] H. Suzuki, Segregation of solute atoms to stacking faults, J. Phys. Soc. Jpn. **17**, 322 (1962).

[13] D. Finkenstadt and D. D. Johnson, Solute/defect-mediated pathway for rapid nanoprecipitation in solid solutions: γ surface analysis in fcc Al-Ag, Phys. Rev. B **73**, 024101 (2006).

[14] S. A. Kibey, L. L. Wang, J. B. Liu, H. T. Johnson, H. Sehitoglu, and D. D. Johnson, Quantitative prediction of twinning stress in fcc alloys: Application to Cu-Al, Phys. Rev. B **79**, 214202 (2009).

[15] D. B. Miracle and O. N. Senkov, A critical review of high entropy alloys and related concepts, Acta Mater. **122**, 448 (2017).

[16] M. Widom, W. P. Huhn, S. Maiti, and W. Steurer, Hybrid Monte Carlo/molecular dynamics simulation of a refractory metal high entropy alloy, Metall. Mater. Trans. A **45**, 196 (2014).

[17] F. Tian, L. K. Varga, N. Chen, J. Shen, and L. Vitos, Empirical design of single phase high-entropy alloys with high hardness, Intermetallics **58**, 1 (2015).

[18] P. Bhattacharjee, G. Sathiaraj, M. Zaid, J. Gatti, C. Lee, C.-W. Tsai, and J.-W. Yeh, Microstructure and texture evolution during annealing of equiatomic CoCrFeMnNi high-entropy alloy, J. Alloys Compd. **587**, 544 (2014).

[19] H. Zhang, Y.-Z. He, Y. Pan, and S. Guo, Thermally stable laser cladded CoCrCuFeNi high-entropy alloy coating with low stacking fault energy, J. Alloys Compd. **600**, 210 (2014).

[20] S. Zhao, Y. Osetsky, G. M. Stocks, and Y. Zhang, Local-environment dependence of stacking fault energies in concentrated solid-solution alloys, npj Comput. Mater. **5**, 13 (2019).

[21] M. Shih, J. Miao, M. Mills, and M. Ghazisaeidi, Stacking fault energy in concentrated alloys, Nat. Commun. **12**, 3590 (2021).

[22] Y. Ikeda, F. Körmann, I. Tanaka, and J. Neugebauer, Impact of chemical fluctuations on stacking fault energies of CrCoNi and CrMnFeCoNi high entropy alloys from first principles, Entropy **20**, 655 (2018).

[23] H. Zheng, L. T. W. Fey, X.-G. Li, Y.-J. Hu, L. Qi, C. Chen, S. Xu, I. J. Beyerlein, and S. P. Ong, Multi-scale investigation of short-range order and dislocation glide in the MoNbTi and TaNbTi multi-principal element alloys, npj Comput. Mater. **9**, 89 (2023).

[24] J. Ding, Q. Yu, M. Asta, and R. O. Ritchie, Tunable stacking fault energies by tailoring local chemical order in CrCoNi medium-entropy alloys, Proc. Natl. Acad. Sci. USA **115**, 8919 (2018).

[25] R. Zhang, S. Zhao, J. Ding, Y. Chong, T. Jia, C. Ophus, M. Asta, R. O. Ritchie, and A. M. Minor, Short-range order and its impact on the CrCoNi medium-entropy alloy, Nature (London) **581**, 283 (2020).

[26] Y. Wu, F. Zhang, X. Yuan, H. Huang, X. Wen, Y. Wang, M. Zhang, H. Wu, X. Liu, H. Wang *et al.*, Short-range ordering and its effects on mechanical properties of high-entropy alloys, J. Mater. Sci. Technol. **62**, 214 (2021).

[27] B. L. Gyorffy and G. M. Stocks, Concentration waves and fermi surfaces in random metallic alloys, Phys. Rev. Lett. **50**, 374 (1983).

[28] A. Zaddach, C. Niu, C. Koch, and D. Irving, Mechanical properties and stacking fault energies of NiFeCrCoMn high-entropy alloy, JOM **65**, 1780 (2013).

[29] Q. Ding, Y. Zhang, X. Chen, X. Fu, D. Chen, S. Chen, L. Gu, F. Wei, H. Bei, Y. Gao *et al.*, Tuning element distribution, structure and properties by composition in high-entropy alloys, Nature (London) **574**, 223 (2019).

[30] Z. Li, K. G. Pradeep, Y. Deng, D. Raabe, and C. C. Tasan, Metastable high-entropy dual-phase alloys overcome the strength–ductility trade-off, Nature (London) **534**, 227 (2016).

[31] C. Wagner, A. Ferrari, J. Schreuer, J.-P. Couzinié, Y. Ikeda, F. Körmann, G. Eggeler, E. P. George, and G. Laplanche, Effects of Cr/Ni ratio on physical properties of Cr-Mn-Fe-Co-Ni high-entropy alloys, Acta Mater. **227**, 117693 (2022).

[32] C. Wagner and G. Laplanche, Effects of stacking fault energy and temperature on grain boundary strengthening, intrinsic lattice strength and deformation mechanisms in CrMnFeCoNi high-entropy alloys with different Cr/Ni ratios, Acta Mater. **244**, 118541 (2023).

[33] H. Zhang, H. Yan, H. Yu, Z. Ji, Q. Hu, and N. Jia, The effect of Co and Cr substitutions for Ni on mechanical properties and plastic deformation mechanism of FeMnCoCrNi high entropy alloys, J. Mater. Sci. Technol. **48**, 146 (2020).

[34] A. Dick, T. Hickel, and J. Neugebauer, The effect of disorder on the concentration-dependence of stacking fault energies in $Fe_{1-x}Mn_x$-a first principles study, Steel Res. Int. **80**, 603 (2009).

[35] G. Arora and D. S. Aidhy, Machine learning enabled prediction of stacking fault energies in concentrated alloys, Metals **10**, 1072 (2020).

[36] S. Xu, E. Hwang, W.-R. Jian, Y. Su, and I. J. Beyerlein, Atomistic calculations of the generalized stacking fault energies in two refractory multi-principal element alloys, Intermetallics **124**, 106844 (2020).

[37] F. Wang, G. H. Balbus, S. Xu, Y. Su, J. Shin, P. F. Rottmann, K. E. Knipling, J.-C. Stinville, L. H. Mills, O. N. Senkov *et al.*, Multiplicity of dislocation pathways in a refractory multiprincipal element alloy, Science **370**, 95 (2020).

[38] A. Van de Walle, P. Tiwary, M. De Jong, D. Olmsted, M. Asta, A. Dick, D. Shin, Y. Wang, L.-Q. Chen, and Z.-K. Liu, Efficient stochastic generation of special quasirandom structures, Calphad **42**, 13 (2013).

[39] See Supplemental Material at http://link.aps.org/supplemental/10.1103/PhysRevMaterials.7.L110401 for further notes and graphs.

[40] P. E. Blöchl, Projector augmented-wave method, Phys. Rev. B **50**, 17953 (1994).

[41] G. Kresse and D. Joubert, From ultrasoft pseudopotentials to the projector augmented-wave method, Phys. Rev. B **59**, 1758 (1999).

[42] J. P. Perdew, K. Burke, and M. Ernzerhof, Generalized gradient approximation made simple, Phys. Rev. Lett. **77**, 3865 (1996).

[43] S. Yin, Y. Zuo, A. Abu-Odeh, H. Zheng, X.-G. Li, J. Ding, S. P. Ong, M. Asta, and R. O. Ritchie, Atomistic simulations of dislocation mobility in refractory high-entropy alloys and the effect of chemical short-range order, Nat. Commun. **12**, 4873 (2021).

[44] S. Plimpton, Fast parallel algorithms for short-range molecular dynamics, J. Comput. Phys. **117**, 1 (1995).

[45] Z. Pei, An overview of modeling the stacking faults in lightweight and high-entropy alloys: Theory and application, Mater. Sci. Eng. A **737**, 132 (2018).

[46] S. Shang, W. Wang, B. Zhou, Y. Wang, K. Darling, L. Kecskes, S. Mathaudhu, and Z. Liu, Generalized stacking fault energy, ideal strength and twinnability of dilute Mg-based alloys: A

first-principles study of shear deformation, Acta Mater. **67**, 168 (2014).

[47] P. Tu, Y. Zheng, C. Zhuang, X. Zeng, and H. Zhu, A high-throughput computation framework for generalized stacking fault energies of pure metals, Comput. Mater. Sci. **159**, 357 (2019).

[48] J.-A. Yan, C.-Y. Wang, and S.-Y. Wang, Generalized-stacking-fault energy and dislocation properties in *bcc* Fe: A first-principles study, Phys. Rev. B **70**, 174105 (2004).

[49] W. A. Harrison, *Electronic Structure and the Properties of Solids: The Physics of the Chemical Bond* (Courier Corporation, North Chelmsford, MA, 2012).

[50] S. Shi, L. Zhu, H. Zhang, Z. Sun, and R. Ahuja, Mapping the relationship among composition, stacking fault energy and ductility in Nb alloys: A first-principles study, Acta Mater. **144**, 853 (2018).

[51] J. Zhang, Y. Dou, G. Liu, and Z. Guo, First-principles study of stacking fault energies in Mg-based binary alloys, Comput. Mater. Sci. **79**, 564 (2013).

[52] C. Wang, H.-Y. Zhang, H.-Y. Wang, G.-J. Liu, and Q.-C. Jiang, Effects of doping atoms on the generalized stacking-fault energies of Mg alloys from first-principles calculations, Scr. Mater. **69**, 445 (2013).

[53] Q.-M. Hu and R. Yang, Basal-plane stacking fault energy of hexagonal close-packed metals based on the Ising model, Acta Mater. **61**, 1136 (2013).

[54] C. Wang, W. Zu, H. Wang, and Y. Wang, First-principles study on stacking fault energy of γ-Fe–Mn alloys, Met. Mater. Int. **27**, 3205 (2021).

[55] B. Wei, W. Wu, M. Gong, S. Yu, S. Ni, M. Song, and J. Wang, Influence of lowering basal stacking fault energy on twinning behaviours, Acta Mater. **245**, 118637 (2023).

[56] M. Turchanin and P. Agraval, Cohesive energy, properties, and formation energy of transition metal alloys, Powder Metall. Met. Ceram. **47**, 26 (2008).

[57] M. Cyrot and F. Cyrot-Lackmann, Energy of formation of binary transitional alloys, J. Phys. F: Met. Phys. **6**, 2257 (1976).

[58] A. Pasturel, C. Colinet, and P. Hicter, Heats of formation in transition intermetallic alloys, Acta Metall. **32**, 1061 (1984).

[59] A. V. Ruban, H. L. Skriver, and J. K. Nørskov, Crystal-structure contribution to the solid solubility in transition metal alloys, Phys. Rev. Lett. **80**, 1240 (1998).

[60] J. R. Kitchin, J. K. Nørskov, M. A. Barteau, and J. G. Chen, Role of strain and ligand effects in the modification of the electronic and chemical properties of bimetallic surfaces, Phys. Rev. Lett. **93**, 156801 (2004).

[61] S. K. Nayak, C. J. Hung, R. J. Hebert, and S. P. Alpay, Atomistic origins of Guinier-Preston zone formation and morphology in Al-Cu and Al-Ag alloys from first principles, Scr. Mater. **162**, 235 (2019).

[62] Y.-H. Li, H.-B. Zhou, L. Liang, N. Gao, H. Deng, F. Gao, G. Lu, and G.-H. Lu, Transition from ductilizing to hardening in tungsten: The dependence on rhenium distribution, Acta Mater. **181**, 110 (2019).

[63] C. Yang and L. Qi, *Ab initio* calculations of ideal strength and lattice instability in W-Ta and W-Re alloys, Phys. Rev. B **97**, 014107 (2018).

[64] J. Zhang, Y. Hu, Q. Wei, Y. Xiao, P. Chen, G. Luo, and Q. Shen, Microstructure and mechanical properties of Re_xNbMoTaW high-entropy alloys prepared by arc melting using metal powders, J. Alloys Compd. **827**, 154301 (2020).

[65] S. Maiti and W. Steurer, Structural-disorder and its effect on mechanical properties in single-phase TaNbHfZr high-entropy alloy, Acta Mater. **106**, 87 (2016).